





Cross-correlating Dark Sirens and Galaxies: Constraints on H_0 from GWTC-3 of LIGO–Virgo–KAGRA

Suvodip Mukherjee^{1,2}, Alex Krolewski^{2,3}, Benjamin D. Wandelt^{4,5} , and Joseph Silk^{4,6,7} ¹ Department of Astronomy and Astrophysics, Tata Institute of Fundamental Research, Mumbai 400005, India; mukherje.suvodip@gmail.com² Perimeter Institute for Theoretical Physics, 31 Caroline Street North, Waterloo, ON N2L 2Y5, Canada; akrolews@uwaterloo.ca³ AMTD Fellow, Waterloo Centre for Astrophysics, University of Waterloo, Waterloo, ON N2L 3G1, Canada⁴ Institut d’Astrophysique de Paris, UMR 7095, CNRS, Sorbonne Université, 98bis Boulevard Arago, 75014 Paris, France; wandelt@iap.fr, joseph.silk@physics.ox.ac.uk, silk@iap.fr⁵ Center for Computational Astrophysics, Flatiron Institute, 162 5th Avenue, New York, NY 10010, USA⁶ Beecroft Institute for Cosmology and Particle Astrophysics, University of Oxford, Keble Road, Oxford OX1 3RH, UK⁷ The Johns Hopkins University, Department of Physics & Astronomy, Bloomberg Center for Physics and Astronomy, Room 366, 3400 N. Charles Street, Baltimore, MD 21218, USA

Received 2024 April 30; revised 2024 August 31; accepted 2024 September 14; published 2024 November 4

Abstract

We apply the cross-correlation technique to infer the Hubble constant (H_0) of the Universe using gravitational-wave (GW) sources without electromagnetic counterparts (dark sirens) from the third GW Transient Catalog (GWTC-3) and the photometric galaxy surveys 2MPZ and WISE-SuperCOSMOS, and combine these with the bright siren measurement of H_0 from GW170817. The posterior on H_0 with only dark sirens is uninformative due to the small number of well-localized GW sources. Using the eight well-localized dark sirens and the binary neutron star GW170817 with electromagnetic counterpart, we obtain a value of the Hubble constant $H_0 = 75.4_{-6}^{+11}$ km s⁻¹ Mpc⁻¹ (median and 68.3% equal-tailed interval) after marginalizing over the matter density and the GW bias parameters. This measurement is mostly driven by the bright siren measurement, and any constraint from dark sirens is not statistically significant. In the future, with more well-localized GW events, the constraints on expansion history will improve.

Unified Astronomy Thesaurus concepts: [Cosmology \(343\)](#); [Observational cosmology \(1146\)](#)

1. Introduction

Discovery of gravitational waves (GWs; B. P. Abbott et al. 2016) by the LIGO–Virgo–KAGRA (LVK) collaboration (F. Acernese et al. 2014, 2019; LIGO Scientific Collaboration et al. 2015; D. V. Martynov et al. 2016; Kagra Collaboration et al. 2019; T. Akutsu et al. 2021) has opened a new observational window to study the cosmos using transient sources such as binary neutron stars, binary black holes (BBHs), and neutron star–black hole mergers. GW sources are uniquely accurate tracers of the luminosity distance. They can therefore be used to measure the expansion history of the Universe (B. F. Schutz 1986). This fact has earned GW sources the name *standard sirens*. However, one of the key ingredients required to measure the expansion history using GW sources is an independent measurement (or inference) of the GW source redshifts.

In the absence of electromagnetic counterparts, a promising way to infer the GW source redshifts is through spatial cross-correlation of the GW sources with galaxies of known redshift. This is an application of the clustering redshift method (J. A. Newman 2008; B. Menard et al. 2013; S. J. Schmidt et al. 2013) that has also been used for the calibration of photometric redshifts for weak lensing surveys (R. Cawthon et al. 2022; M. Gatti et al. 2022; M. M. Rau et al. 2023), relying on the fact that sources with an unknown redshift distribution (i.e., the GW sources) will cluster more strongly when cross-

correlated with galaxies at the peak of the unknown sources’ redshift distribution.

By using the clustering redshift of the GW sources (M. Oguri 2016; S. Mukherjee & B. D. Wandelt 2018; S. Bera et al. 2020; S. Mukherjee et al. 2020, 2021b), we can measure the cosmic expansion history after marginalizing over the GW bias parameters encoding the redshift evolution of the bias. Apart from cross-correlation techniques, statistical host identification (B. F. Schutz 1986; M. Soares-Santos et al. 2019; R. Abbott et al. 2020) and GW mass distribution (S. R. Taylor et al. 2012; W. M. Farr et al. 2019; S. Mastrogiovanni et al. 2021) can also be used to infer redshifts for BBHs. However, the mass distribution of the BBHs can have an intrinsic redshift dependence that influences parameter estimation if the full mass distribution gets affected (S. Mukherjee 2022; J. M. Ezquiaga & D. E. Holz 2022).

LVK dark standard sirens have been used to measure the expansion history using O1+O2 data (B. P. Abbott et al. 2021) and O1+O2+O3 data (R. Abbott et al. 2023), in tandem with GLADE (G. Dálya et al. 2018) and GLADE+ (G. Dálya et al. 2022) for statistical host identification for a fixed cosmological population. The latest LVK measurement yields $H_0 = 68_{-6}^{+8}$ km s⁻¹ Mpc⁻¹ (68.3% highest density interval, HDI) after combining with the bright siren GW170817 (R. Abbott et al. 2023). Other independent measurements of H_0 using statistical host identification have also been performed on the GW data (A. Finke et al. 2021; A. Palmese et al. 2023).

In this paper, we apply the cross-correlation technique on the GWTC-3 catalog of the LVK collaboration (R. Abbott et al. 2023) and the photometric galaxy surveys 2MPZ (M. Bilicki et al. 2014) and WISE-SuperCOSMOS (WSC; M. Bilicki et al. 2016) and attempt to infer the Hubble constant H_0 assuming

flat Lambda cold dark matter (Λ CDM) as the baseline model. Though currently, we cannot detect clustering between GW sources and galaxies due to the limited number of GW sources and large sky localization error, this is the first application of this technique on data. The current measurement is limited by the lack of high-redshift galaxies and the small number of well-localized GW sources. However, the cross-correlation technique does not depend on assumptions about the position of the lower limit of the pair-instability supernovae (PISNe) mass gap to measure the Hubble constant and provides an independent technique to infer the value of the Hubble constant after marginalizing over assumptions for the GW source population. Further, we note that the cross-correlation technique does not depend on assumptions about the completeness of the underlying galaxy survey, as in the statistical host identification method.

2. Method

GW sources and galaxies are tracers of the underlying dark matter distribution, with their power spectra related to the matter power spectrum by a linear bias on large scales. The angular cross-correlation between the GW sources and galaxies with known redshifts is therefore proportional to the linear bias of the GW sources, the (known) linear galaxy bias and redshift distribution, and, crucially, the unknown GW redshift distribution (J. A. Newman 2008; B. Menard et al. 2013; S. J. Schmidt et al. 2013). In this way, by measuring the cross-correlation of the GW sources and galaxies, we can infer the redshift distribution of the GW sources, as shown by S. Mukherjee & B. D. Wandelt (2018) and S. Mukherjee et al. (2021b, 2021c).

From the observed spatial distribution of GW sources (or galaxies) $n_X(\theta, \phi)$, we can construct a density map as

$$\delta^X(\theta, \phi) = \frac{n_X(\theta, \phi)}{\bar{n}_X} - 1, \quad (1)$$

where \bar{n}_X is the mean density and $X \in \{\text{GW}, g\}$. The angular correlation between a galaxy map and a GW map in the spherical harmonic basis can be written as

$$\hat{C}_\ell^{XY} = \frac{\sum_m \tilde{\delta}_{\ell m}^X \tilde{\delta}_{\ell m}^{*Y}}{2l + 1}, \quad (2)$$

where \hat{C}_ℓ^{XY} denotes the pseudo auto (for $X = Y$) and cross (for $X \neq Y$) angular power spectrum obtained from the masked density maps, denoted by $\tilde{\delta}$. One can construct the binned average power spectrum as $\hat{C}_{\ell_b}^{XY} = \sum_{\ell \in \ell_b} W_\ell C_\ell^{XY}$, where W_ℓ denotes the normalized window function. The corresponding covariance matrix Σ for the angular power spectrum in the Gaussian limit can be written as

$$\Sigma_{\ell\ell'} = \delta_{\ell\ell'} \frac{(C_\ell^{XX} + n_\ell^X)(C_\ell^{YY} + n_\ell^Y) + C_\ell^{XY}}{(2\ell + 1)f_{\text{sky}}\Delta\ell}, \quad (3)$$

where n_ℓ^X denotes the shot noise for tracer X , equal to the inverse of its number density. For the cross-power spectrum, the shot noise is zero. $f_{\text{sky}} \equiv \Omega_s/4\pi$ denotes the overlapping sky fraction between GW sources and galaxy catalog, and $\Delta\ell$ denotes the bin width in ℓ -space over which we estimate the band-averaged power spectrum. Choosing a large bin width makes it possible to reduce the correlation between different multipoles arising from the mask.

We estimate the cosmological parameters, Hubble constant H_0 and matter density Ω_m , along with the GW bias parameter $b_{\text{GW}}(z) = b_{\text{GW}}(1 + z)^\alpha$ using a Bayesian framework based on previous works (S. Mukherjee et al. 2021b, 2021c; C. Cigarrán Díaz & S. Mukherjee 2022). The posterior on the parameters given the GW data $\mathcal{D}_{\text{GW}} \in \{d_i^j, \Delta\Omega^i\}$ is composed of the luminosity distance d_i^j and sky map $\Delta\Omega^i$ of the GW sources (denoted by the index i). These sources are then distributed in N_{GW} bins of the GW luminosity distance. The galaxy data for N_{gal} galaxies are $\mathbf{d}_g \in \{z^j, \text{R.A.}^j, \text{decl.}^j\}$ composed of the galaxy redshift and the sky position denoted by R.A. and decl., where $j \in \{1, N_{\text{gal}}\}$. After marginalizing over the nuisance parameters $\Theta_n \in \{b_{\text{GW}}, \alpha\}$, we can write the posterior on the cosmological parameters (denoted by Θ_c) as

$$\begin{aligned} \mathcal{P}(\Theta_c | \mathcal{D}_{\text{GW}}, \mathbf{d}_g) \propto & \iint d\Theta_n dz \prod_{i=1}^{N_{\text{GW}}} \Pi(z)\Pi(\Theta_n)\Pi(\Theta_c) \\ & \times \mathcal{L}(\mathcal{D}_{\text{GW}} | \{C_\ell^{gg}(z)\}, \Theta_n, \mathbf{d}_g(z)) \\ & \times \mathcal{P}(\mathbf{d}_g(z) | \{C_\ell^{gg}(z)\}) \\ & \times \mathcal{P}(\{d_i^j\}_{\text{GW}} | z, \Theta_c, \{\hat{\theta}^i, \hat{\phi}^i\}_{\text{GW}}), \end{aligned} \quad (4)$$

where the likelihood $\mathcal{L}(\mathcal{D}_{\text{GW}} | \{C_\ell^{gg}(z)\}, \Theta_n, \mathbf{d}_g(z))$ is written as

$$\begin{aligned} \mathcal{L}(\mathcal{D}_{\text{GW}} | \{C_\ell^{gg}(z)\}, \Theta_n, \mathbf{d}_g(z)) = & \frac{1}{\sqrt{2\pi \Sigma_{\ell_b, \ell_b}^{-1}}} \\ & \times \exp\left(-0.5 \sum_{\ell_b, \ell_b}^{\ell_{\text{max}}} D(\ell_b, z) \Sigma_{\ell_b, \ell_b}^{-1} D(\ell_b, z)\right). \end{aligned} \quad (5)$$

Here, ℓ_{max} denotes the maximum value of the multipoles that can be used (which depends on the sky localization error) and

$$D(\ell, z) = \hat{C}_\ell^{\text{GW}g}(z) - C_\ell^{\text{GW}g}(z), \quad (6)$$

where $C_\ell^{\text{GW}g}$ is the theoretical model for the GW–galaxy cross-correlation and $\hat{C}_\ell^{\text{GW}g}$ is the measured cross-correlation. In this analysis, we have only considered the diagonal covariance matrix, leading to simplification in Equation (5). However, in the future with more GW sources, considering the full covariance matrix will be appropriate.

The angular cross-correlation power spectrum $\hat{C}_\ell^{\text{GW}g}(z)$ is obtained from cross-correlating GW sources detected above a network-matched filtering signal-to-noise ratio (SNR) with galaxy catalogs $\mathbf{d}_g(z)$. The theoretical angular cross-power spectrum is written in terms of the measured galaxy auto-power spectrum $C_\ell^{gg}(z)$, the galaxy bias $b_g(z)$, and GW bias $b_{\text{GW}}(z)$ as

$$C_\ell^{\text{GW}g}(z) = \frac{b_{\text{GW}}(z)}{b_g(z)} C_\ell^{gg}(z). \quad (7)$$

We describe in Appendix A in detail the procedure followed to measure galaxy autocorrelation and galaxy bias. The term $\mathcal{P}(\mathbf{d}_g(z) | \{C_\ell^{gg}(z)\})$ denotes the galaxy density field given the auto-power spectrum $C_\ell^{gg}(z)$. The likelihood on the luminosity distance given the cosmological parameters Θ_c and redshift is denoted by $\mathcal{P}(\{d_i^j\}_{\text{GW}} | z, \Theta_c, \{\hat{\theta}^i, \hat{\phi}^i\}_{\text{GW}})$, and the priors on the redshift, cosmological parameters, and nuisance parameters are denoted by $\Pi(z)$, $\Pi(\Theta_c)$, and $\Pi(\Theta_n)$ respectively.

We include only large scales $\ell \leq 30$ and consider different choices of bins $\Delta\ell = 5$ and 15 in the analysis. The smallest

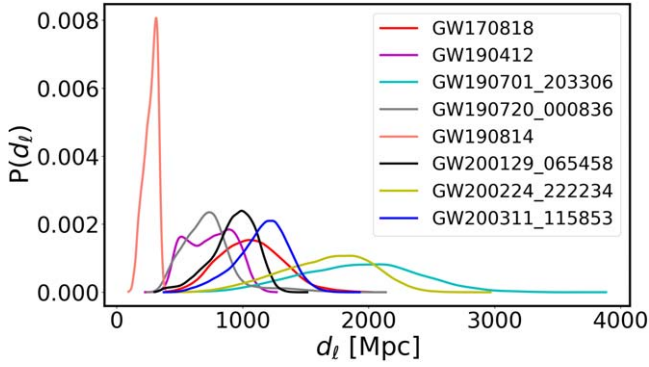


Figure 1. The luminosity distance of the eight selected GW sources from GWTC-3.

scale used, $\ell_{\max} = 30$, is chosen due to the poor sky localization of the GW sources, which imposes a beam that effectively smears out smaller scales. We do not use the first ℓ -bin in the analysis to minimize low- ℓ contamination. Our results will also depend on z_{\max} , the maximum redshift of the flat prior on GW source redshift, $\Pi(z)$, i.e., the maximum redshift up to which Equation (4) is integrated. We also choose two different values of z_{\max} , namely $z_{\max} = 0.5$ and $z_{\max} = 2$ in the analysis.

3. GW Catalog and Galaxy Catalog Selection Function

In this analysis, we use the publicly available catalog GWTC-3 of GWs detected by the LVK collaboration (R. Abbott et al. 2023). As the most constraining estimations of cosmological parameters can be made from sources that have a high matched-filtering SNR, we select samples from GWTC-3 with $\text{SNR} \geq 11$. Also, as the cross-correlation technique is most effective for sources with better sky localization error, we further select sources with sky localization error $\Delta\Omega \leq 30 \text{ deg}^2$ at 68.3% credible interval. These two selections lead to a total of eight GW events, namely GW170818, GW190412, GW190814, GW190701_203306, GW190720_000836, GW200129_065458, GW200224_222234, and GW200311_115853.

The posteriors on the luminosity distance are shown in Figure 1 and the sky map of the GW sources and the sky mask are shown in Figure 2. The spatial distribution of the GW sources in the sky with good sky localization error depends on the number of GW detectors operational at the time of observation, the noise and antenna pattern of the individual detectors, and also on the properties of the individual GW sources. For sources with higher masses, the sky localization error is improved. Also, for sources with unequal masses, the sky localization error will be better. In our analysis, we consider only the fraction of the sky ($f_{\text{sky}} \sim 2\%$) that is allowed by the well-localized sources for which the sky localization error is less than 30 deg^2 for O3 sensitivity of GW detectors.

We construct three GW maps from the selected GW samples composed of Set-1 (GW190814), Set-2 (GW170818, GW190412, GW190720_000836, GW200129_065458, GW200311_115853), and Set-3 (GW190701_203306, GW200224_222234). These maps are constructed based on the distribution of luminosity distance of the GWs. Sources with a similar maximum value of the posterior distribution are combined to enhance the cross-correlation signal.

Galaxy catalog and selection function. We use galaxies from the Two Micron All Sky Survey (2MASS) Photometric

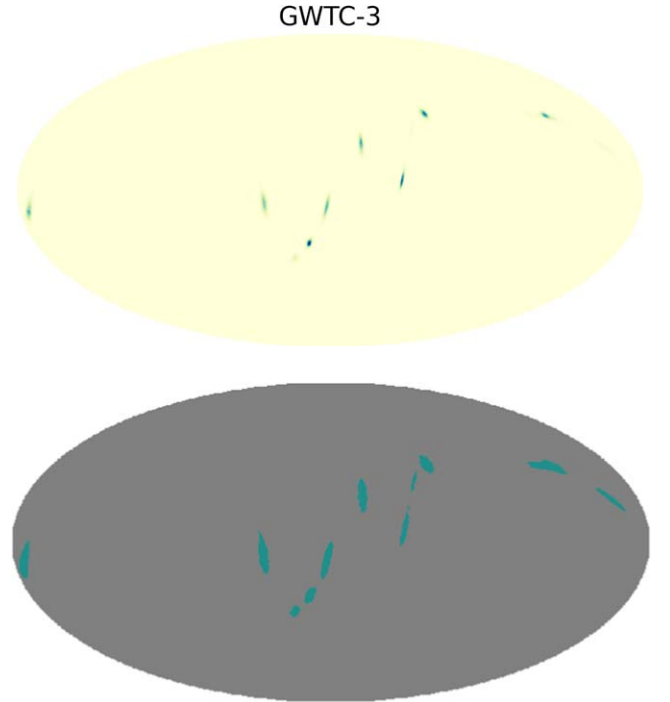


Figure 2. The sky map in equatorial coordinates of the eight selected GW sources from GWTC-3 (top) and the GW sky mask (bottom) used in the analysis.

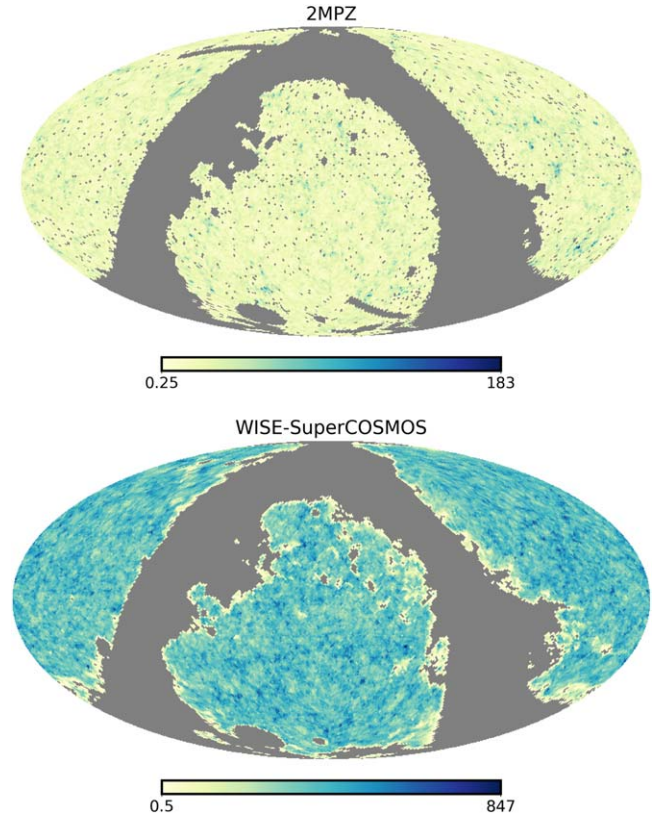


Figure 3. The sky map along with the mask (gray) in equatorial coordinates of 2MPZ (top) and WSC (bottom).

Redshift catalog (2MPZ; M. Bilicki et al. 2014) and Wide-field Infrared Survey Explorer (WISE) cross SuperCOSMOS Photometric Redshift catalog (WSC; M. Bilicki et al. 2016). The sky maps of the galaxies are shown in Figure 3. The details

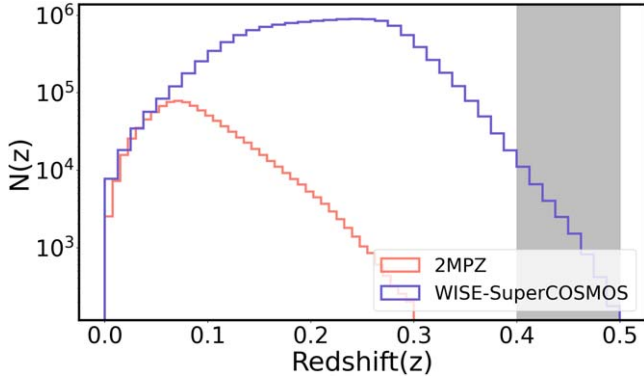


Figure 4. The redshift distribution of the 2MPZ (in orange) and WSC (in blue) galaxies. The shaded region shows the redshift range that is shot-noise-dominated.

of both these catalogs can be found in M. Bilicki et al. (2014, 2016). The choice of mask⁸ for the 2MPZ (M. Bilicki et al. 2014) and WSC (M. Bilicki et al. 2016) galaxy surveys left nearly 65% of the sky. DeCALs (R. Zhou et al. 2021) is another survey that would be desirable for this analysis, as it lies at higher redshift than WSC and has considerably lower stellar contamination. However, DeCALs is focused on the Northern sky, and while the sky fraction is still high ($\sim 50\%$) it unfortunately misses four out of the eight GW events. As a result, we use only 2MPZ and WSC in this paper.

The redshift distributions of 2MPZ and WSC are shown in Figure 4 in orange and blue respectively. At $z < 0.1$ we use 2MPZ despite its lower number density, as it has more precise photometric redshifts ($\sigma_z = 0.015$; M. Bilicki et al. 2014) and far less stellar contamination. For $z > 0.1$, we use WSC exclusively (having $\sigma_z/(1+z) = 0.033$; M. Bilicki et al. 2016). At $0.3 < z < 0.4$, WSC clustering is shot-noise-dominated at $\ell > 60$, and for $z > 0.4$ it is shot-noise-dominated at all ℓ . We still measure galaxy clustering at $0.4 < z < 0.5$, albeit with increased errors (total SNR ~ 4.7 , after subtracting shot noise, over the relevant scales $10 < \ell < 40$), but exclude $z > 0.5$, where there are very few WSC galaxies. For both surveys, photometric redshifts are trained using the ANNz algorithm (A. A. Collister & O. Lahav 2004), yielding typical redshift errors $\sigma_z = 0.015$ for 2MPZ and $\sigma_z/(1+z) = 0.033$ for WSC.

4. Results

We have adopted the following uniform prior ranges: $\Pi(H_0) = \mathcal{U}[20, 120] \text{ km s}^{-1} \text{ Mpc}^{-1}$, $\Pi(\Omega_m) = \mathcal{U}[0.1, 0.4]$, $\Pi(z) = \mathcal{U}[0, z_{\max}]$, $\Pi(b_{\text{GW}}) = \mathcal{U}[0.1, 6]$, and $\Pi(\alpha) = \mathcal{U}[-2, 2]$, and a flat Λ CDM cosmological model. In this analysis, we have used the emcee: The MCMC Hammer (D. Foreman-Mackey et al. 2013) for estimating the posteriors of the parameter with nwalker = 40 and chain size 10^4 . We have shown results for two different choices of redshift bin width, $\Delta z = 0.05$ and $\Delta z = 0.1$, which are roughly 1.5 and 3 times the WSC photo- z error respectively. We also consider two different choices of bins, $\Delta \ell = 5$ and 15, and two different values of z_{\max} , namely $z_{\max} = 0.5$ and $z_{\max} = 2$. $z_{\max} = 0.5$ is the maximum redshift of the galaxy catalog; however, the GW sources may lie at higher redshift. $z_{\max} = 2$ is sufficiently high; beyond it detection of sources with matched-filtering SNR > 12 for a prior range of H_0 of $[20, 120] \text{ km s}^{-1} \text{ Mpc}^{-1}$ with O3 detector sensitivity will not

⁸ The details for the construction of the mask are given in Appendix B.

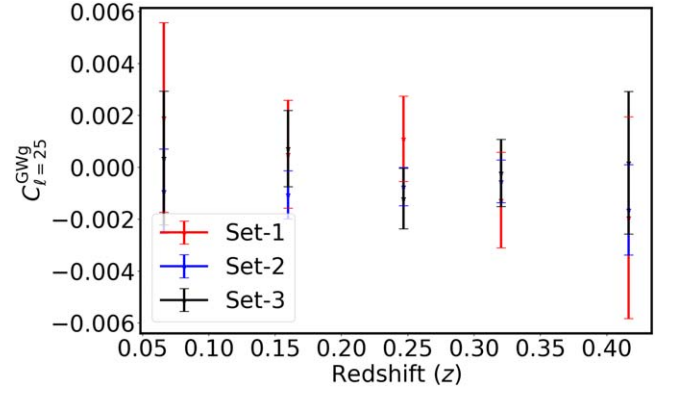


Figure 5. The band-averaged cross-correlation power spectrum between GW sources and galaxies with a $\Delta \ell = 15$ bin width and $\Delta z = 0.1$ is shown for three different maps of the GW sources: Set-1 (GW190814), Set-2 (GW170818, GW1901412, GW190720_000836, GW2001129_065458, GW200311_115853), and Set-3 (GW190701_203306, GW200224_222234) composed from the selected eight events, as a function of the median value of the redshift bin.

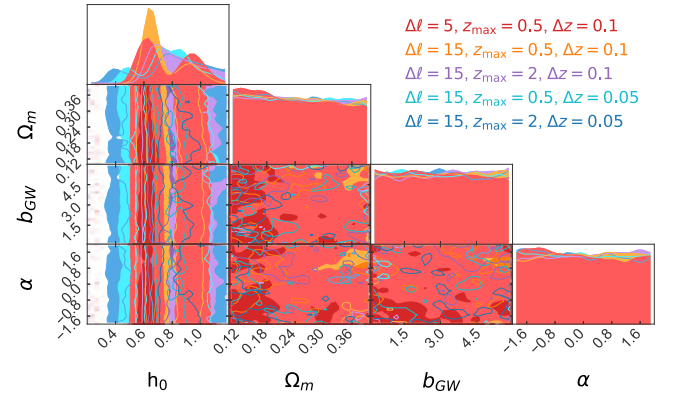


Figure 6. The joint constraints on $H_0 = 100h_0 \text{ km s}^{-1} \text{ Mpc}^{-1}$, Ω_m , and $b_{\text{GW}}(z) = b_{\text{GW}}(1+z)^\alpha$ for different choices of bin width $\Delta \ell$, z_{\max} , and Δz .

be feasible for these eight sources with their detector-frame mass parameters. To make sure that the result is not susceptible to the choice of the maximum value of mass (i.e., population-independent), we also checked that our results do not change even when we take $z_{\max} = 4$. A null test validating the technique on a mock random catalog (without any spatial clustering) is shown in Appendix C with the same sky mask as the GW data and galaxy catalog. This shows that our method is unbiased and exhibits no constraints from a random galaxy catalog.

The cross-correlation between the GW sources and galaxies is dominated by shot noise and we do not measure any cross-correlation clustering signal with statistical significance. We show the measured band average cross-correlation signal $\hat{C}_\ell^{\text{GWg}}$ as a function of redshift in Figure 5 for $\Delta \ell = 15$ and $\Delta z = 0.1$ with the three GW maps constructed from the eight events. The diagonal error bars are shown on the measured values. The band average signal shows a signal that is consistent with zero at all the redshift bins.

The joint estimation of the Hubble constant along with the matter density and GW bias parameters are shown in Figure 6. Constraints on the Hubble constant are bimodal, with the median value $H_0 = 82.4^{+23}_{-27} \text{ km s}^{-1} \text{ Mpc}^{-1}$ (the upper and lower limits indicate the 68.3% equal-tailed interval, ETI) for $\Delta z = 0.05$ and the maximum redshift in prior $z_{\max} = 2$. The

Table 1Median and 68.3% ETI Values of H_0 for Dark and Dark+Bright Sirens for z_{\max}

Δl	Δz	z_{\max}	$H_0(\text{dark})$ ($\text{km s}^{-1} \text{Mpc}^{-1}$)	$H_0(\text{dark} + \text{bright})$ ($\text{km s}^{-1} \text{Mpc}^{-1}$)
5	0.1	0.5	71.1^{+27}_{-13}	67.7^{+18}_{-5}
15	0.1	0.5	67.5^{+25}_{-6}	66.9^{+6}_{-4}
15	0.1	2	79.8^{+23}_{-15}	71.0^{+11}_{-6}
15	0.05	0.5	78.5^{+17}_{-21}	73.0^{+11}_{-5}
15	0.05	2	82.4^{+23}_{-27}	75.4^{+11}_{-6}

Note. Different choices are made for parameters such as C_ℓ bin width Δl , redshift bin width Δz , and maximum redshift in the prior z_{\max} . The values for all the choices are consistent with each other within the error bars.

constraints for different choices of Δl , Δz , and z_{\max} are shown in Table 1. Due to the limited number of GW sources, we are not able to detect the cross-correlation signal with galaxies, and hence no statistically significant inference of H_0 is possible currently. The values of the matter density Ω_m and bias parameter $b_{\text{GW}}(z)$ are unconstrained as well.

The posterior on the Hubble constant from only dark sirens is uninformative for all the cases and spans nearly the complete prior range due to the nondetection of the cross-correlation signal. In this first application of the cross-correlation technique on GW data, the measurements of H_0 presented are from a small number of GW sources. As a result, the clustering of the GW sources is not measured with any statistical significance, resulting in a weak estimate of H_0 . The values in Table 1 show that all the estimates are statistically consistent due to large error bars. The measurement in this work agrees with the dark siren measurement including the population assumption of $H_0 = 67^{+13}_{-12} \text{ km s}^{-1} \text{Mpc}^{-1}$ (68.3% HDI) by the LVK collaboration (R. Abbott et al. 2023). This measurement is also affected by poor number statistics (R. Abbott et al. 2023) and systematics related to population assumptions.

To test the robustness of our results, we have checked the following aspects: (i) randomly varied the galaxy bias parameters within their error bars, (ii) enhanced the covariance matrix by a factor of four, (iii) changed the cosmological parameters such as $S_8 \equiv \sigma_8 \sqrt{\Omega_m}$ that is used to fit the galaxy power spectrum C_ℓ^{gg} from $S_8 = 0.832$ (Planck-2018, Planck Collaboration et al. 2020) to the lower value $S_8 = 0.75$ as indicated by the KiDS Collaboration (C. Heymans et al. 2021), (iv) changed the value of $H_0 = 67 \text{ km s}^{-1} \text{Mpc}^{-1}$ to $H_0 = 74 \text{ km s}^{-1} \text{Mpc}^{-1}$ (A. G. Riess et al. 2019) to estimate the galaxy bias parameters, (v) changed the galaxy sample selection by additionally removing WSC sources with a low probability of being galaxies using the support vector machine (SVM) catalog of T. Krakowski et al. (2016), requiring $p_{\text{gal}} > 0.67$, (vi) changed the redshift bin width Δz to 0.05, which is comparable to the photo- z errors, and (vii) changed the maximum redshift z_{\max} in the prior. The posterior on H_0 did not show any significant variation for cases (i)–(v). For scenarios (vi) and (vii), the H_0 posterior shows some variation. As shown in Table 1, the error bars increase with decreasing Δz and increasing z_{\max} . The change with Δz happens because the galaxy redshift kernels begin to overlap due to photo- z errors, violating our assumption that the GW cross-correlations in neighboring bins are uncorrelated. The increase in z_{\max} includes the contribution from higher redshifts in the prior. As there is no support for galaxies beyond $z = 0.5$, there is no information beyond the prior choice. As a result, an allowed large prior on

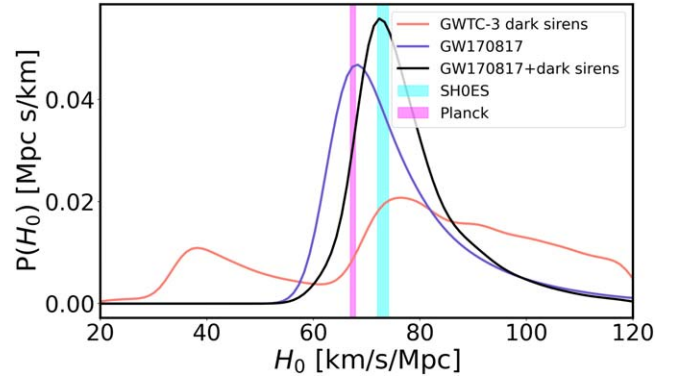


Figure 7. Measurements of Hubble constant H_0 from GWTC-3 dark sirens, bright siren GW170817, and the combination of the two are shown along with the mean and the standard deviation on the measurements from Planck-2018 (Planck Collaboration et al. 2020) and SHOES (A. G. Riess et al. 2022).

redshift (higher z_{\max}) enhances the error at high H_0 in comparison to low H_0 .

By combining the bright standard siren measurement from GW170817 with a better measurement of peculiar velocity (S. Mukherjee et al. 2021a), we show the corresponding posterior on H_0 in Figure 7 with the median value of $H_0 = 75.4^{+11}_{-6} \text{ km s}^{-1} \text{Mpc}^{-1}$ (68.3% ETI) for $\Delta z = 0.05$ and $z_{\max} = 2$. The values of H_0 for other choices of Δz and z_{\max} are mentioned in Table 1. In comparison, the median with 68.3% ETI from GW170817 is $H_0 = 72.8^{+15}_{-8} \text{ km s}^{-1} \text{Mpc}^{-1}$ (S. Mukherjee et al. 2021a)—our combined constraint thus provides a slight improvement on the error bar. The values of the Hubble constant are consistent with each other within about 1σ for all the choices of z_{\max} and Δz . As the GW–galaxy cross-correlation is not detected, the choices of prior on redshift (such as z_{\max} and Δz) mildly impact the results.

In Figure 7 we compare the GW measurements of H_0 with the measurements from Planck, $H_0 = 67.4^{+0.5}_{-0.5} \text{ km s}^{-1} \text{Mpc}^{-1}$ (Planck Collaboration et al. 2020) and with the measurement of $H_0 = 73.04^{+1.05}_{-1.05} \text{ km s}^{-1} \text{Mpc}^{-1}$ from SHOES (A. G. Riess et al. 2022). The current measurements from the dark sirens are not sufficiently constraining yet to resolve the H_0 tension (L. Verde et al. 2019; M. G. Dainotti et al. 2021; E. Di Valentino et al. 2021). Though the systematic uncertainties in our measurement of H_0 are smaller than the statistical uncertainties, in the future with more GW sources and a better galaxy catalog, we will be able to better assess the influence of any systematic uncertainties.

5. Conclusion and Future Outlook

We present the first application of the inference of the Hubble constant H_0 from dark standard sirens using the cross-correlation technique. With the best eight sources available from GWTC-3, we obtain a median value of Hubble constant of $82.4^{+23}_{-27} \text{ km s}^{-1} \text{Mpc}^{-1}$ (68.3% ETI), with the weak constraints on H_0 arising from the nondetection of the GW–galaxy cross-correlation. In the future, with the availability of $z < 0.8$ spectroscopic galaxy catalogs such as DESI (DESI Collaboration et al. 2016) and SPHEREx (O. Doré et al. 2018) (supplemented by $z > 0.8$ spectroscopy from Euclid (A. Blanchard et al. 2020) and photometric redshifts from Vera Rubin Observatory (LSST Science Collaboration et al. 2009)), cross-correlation of the GW sources with galaxies will be a powerful technique to measure the expansion history (S. Mukherjee & B. D. Wandelt 2018; S. Mukherjee et al. 2021b; C. Cigarrán

Díaz & S. Mukherjee 2022) and test the general theory of relativity (S. Mukherjee et al. 2021c). The measurement presented in this analysis reports a value of the Hubble constant that is not influenced by the choice of the PISNe mass gap (R. Farmer et al. 2019). The dependence of GW sources on the galaxy properties through the GW bias parameter is marginalized in this analysis. In the future, with the availability of a few hundred dark sirens, the cross-correlation technique will be able to infer the clustering redshift of sources more accurately, and this will be able to shed further light on the tension in the determinations of the Hubble constant (L. Verde et al. 2019; E. Di Valentino et al. 2021).

Acknowledgments

The authors are thankful to Gergely Dalya for carefully reviewing the manuscript and providing useful comments during the LVK internal review. The authors are also thankful to Maciej Bilicki for providing insightful suggestions on the paper. Research at Perimeter Institute is supported in part by the Government of Canada through the Department of Innovation, Science and Economic Development and by the Province of Ontario through the Ministry of Colleges and Universities. S.M. and B.D.W. are supported by the Simons Foundation. A.K. thanks the AMTD Foundation for its support. This analysis is carried out at the Symmetry computing facility of the Perimeter Institute and the Infinity cluster hosted by Institut d’Astrophysique de Paris. We thank Stephane Rouberol for smoothly running the Infinity cluster. This research has made use of data obtained from the SuperCOSMOS Science Archive, prepared and hosted by the Wide Field Astronomy Unit, Institute for Astronomy, the University of Edinburgh, which is funded by the UK Science and Technology Facilities Council.

The authors would like to thank the LIGO/Virgo/KAGRA scientific collaboration for providing the data. LIGO is funded by the U.S. National Science Foundation. Virgo is funded by the French Centre National de Recherche Scientifique (CNRS), the Italian Istituto Nazionale della Fisica Nucleare (INFN), and the Dutch Nikhef, with contributions by Polish and Hungarian institutes. This material is based upon work supported by NSF’s LIGO Laboratory, which is a major facility fully funded by the National Science Foundation.

Software: Astropy (Astropy Collaboration et al. 2013, 2018), emcee: The MCMC Hammer (D. Foreman-Mackey et al. 2013), Giant-Triangle-Confusogram (S. Bocquet & F. W. Carter 2016), healpy (K. M. Górski et al. 2005; A. Zonca et al. 2019), IPython (F. Pérez & B. E. Granger 2007), Matplotlib (J. D. Hunter 2007), NaMaster (D. Alonso et al. 2019), NumPy (S. van der Walt et al. 2011), and SciPy (E. Jones et al. 2001).

Appendix A Measuring Galaxy Autocorrelation and Bias

A.1. Method

From the auto-power spectrum, we infer the galaxy bias $b_g(z)$ by fitting a simple linear bias times the nonlinear “Halofit” matter power spectrum model (R. Takahashi et al. 2012). We use the NaMaster code (E. Hivon et al. 2002; D. Alonso et al. 2019) to measure pseudo- C_ℓ for each redshift slice, applying a 1° apodization (“ C^1 apodization”; J. Grain et al. 2009) to the galaxy mask. For WSC, we additionally deproject the Schlegel–Finkbeiner–Davis

Table 2
Summary of Bias Results for 2MPZ with $0 < z_{\text{phot}} < 0.1$

Analysis	Bias
B. Stözlner et al. (2018) fix. cosmo.	1.03 ± 0.03
B. Stözlner et al. (2018) marg. cosmo.	1.19 ± 0.028
A. Balaguera-Antolínez et al. (2018)	1.14 ± 0.38
J. A. Peacock & M. Bilicki (2018)	1.18 ± 0.009
D. Alonso et al. (2015)	1.18 ± 0.03
Default	1.18 ± 0.033
Multiply by WSC mask	1.18 ± 0.017
Mask thres. 0.8	1.18 ± 0.016
Mask thres. 0.9	1.22 ± 0.018
Lorentzian dN/dz 1.21 ± 0.032	

Note. Results from the literature are at the top, and our results are at the bottom (below the horizontal line), with several variations in the mask or assumed form of dN/dz .

(D. J. Schlegel et al. 1998) dust extinction map and a stellar density map from Gaia (A. G. A. Brown et al. 2016) to reduce the impact of contamination, following N. Koukoufilippas et al. (2020). We fit the one-parameter bias model to the data in the range $10 < \ell < 40$, with shot noise fixed. For WSC, we additionally allow for systematic variations in the number density from variations in the zero-point between SuperCOSMOS plates. We add a template to the model:

$$C_\ell^{\text{plate}} = A \exp[-2(\ell\theta_{\text{plate}})^2/12] \quad (\text{A1})$$

where θ_{plate} is the plate scale, 5° (N. Koukoufilippas et al. 2020). Finally, we fix the shot noise to the inverse of the angular number density (in steradians) except for the $0.4 < z < 0.5$ bin, where we adjust it downwards by 5% to match the high- ℓ power of C_ℓ^{gg} . For the other bins, we check that $1/\bar{n}_g$ matches the high- ℓ power in C_ℓ^{gg} , and the discrepancies are small compared to the clustering amplitude at $10 < \ell < 40$.

To model the redshift distribution when determining b_g , we convolve the observed photometric redshift distribution with a Gaussian for 2MPZ (A. Balaguera-Antolínez et al. 2018) and a generalized Lorentzian for WSC,

$$P(\delta z) \propto \left(1 + \frac{\delta z^2}{2a^2}\right)^{-a} \quad (\text{A2})$$

(J. A. Peacock & M. Bilicki 2018). The width evolves as a function of redshift, for the Gaussian following

$$\sigma = 0.027 \tanh(-20.78z_p^2 + 7.76z_p + 0.05)/(1 + z_p) \quad (\text{A3})$$

i.e., increasing from 0.0013 at $z_p = 0$ to 0.013 at $z_p = 0.1$; and for the Lorentzian,

$$a(z_c) = -4z_c + 3 \quad (\text{A4})$$

and

$$s(z_c) = 0.04z_c + 0.02 \quad (\text{A5})$$

where z_c is the midpoint of each redshift bin. Other choices for the redshift error (e.g., redshift-independent modified Lorentzian for 2MPZ in M. Bilicki et al. 2014 and J. A. Peacock & M. Bilicki 2018) yield very similar results.

We assume that the galaxy bias is redshift-independent in each bin, and obtain best-fit values of $b_g(z_c = 0.15) = 0.66$, $b_g(z_c =$

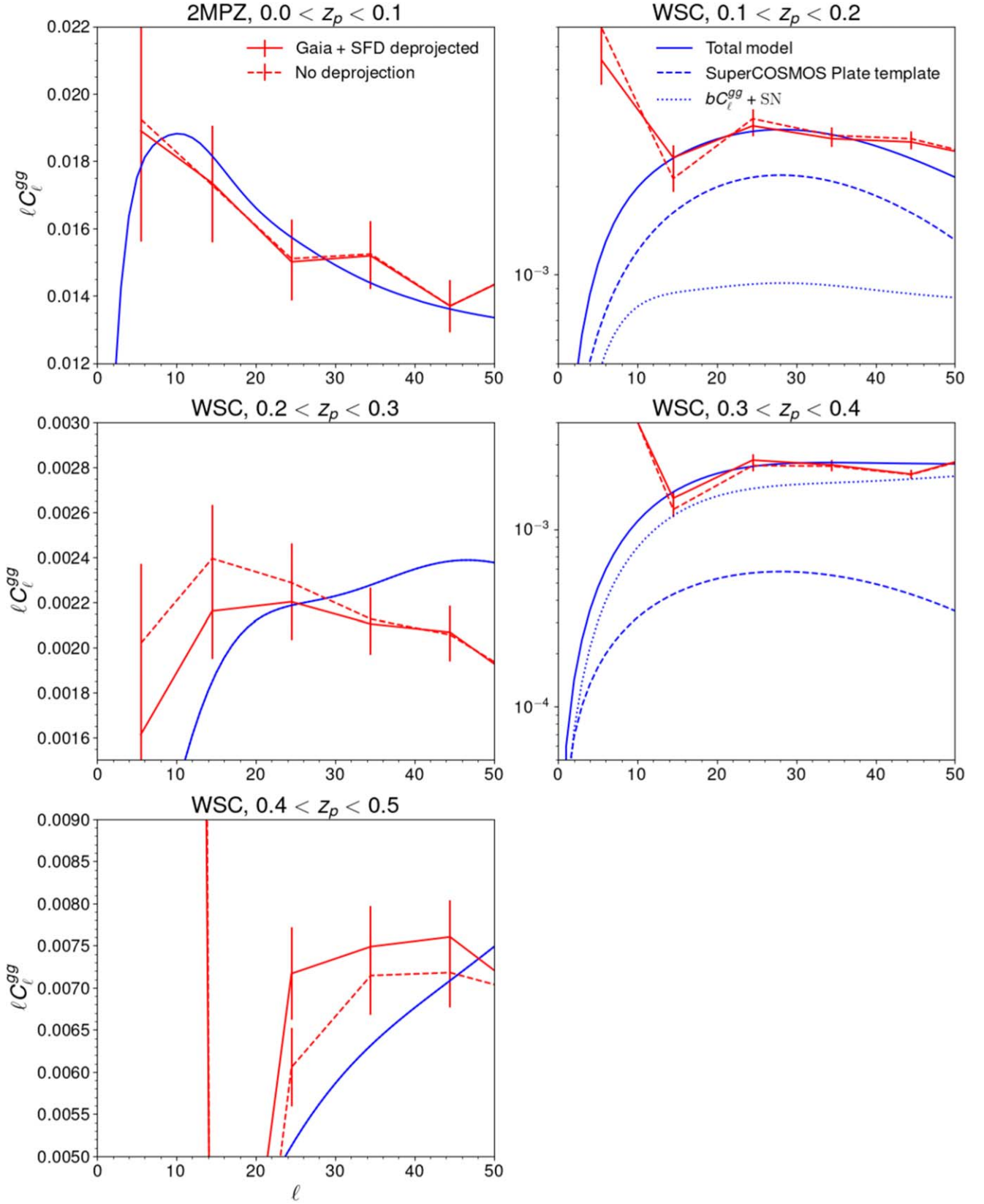


Figure 8. Galaxy autocorrelations in different photometric redshift bins, with the default measurement (deprojecting Gaia stellar template and Schlegel–Finkbeiner–Davis dust map) in solid red, and measurement with no deprojection in dashed red. The model is shown in blue: the total model is in solid blue, which for WSC is the sum of the SuperCOSMOS plate template following N. Koukoufilippas et al. (2020; dashed blue) and bC_l^{gg} plus shot noise (dotted blue).

0.25) = 1.35, $b_g(z_c = 0.35) = 1.76$, and $b_g(z_c = 0.45) = 2.33$. The very low value of b_g in the second bin is driven by the SuperCOSMOS plate template, which is degenerate with the

cosmological contribution due to the limited multipole range considered ($10 < \ell < 40$). Figure 8 shows plots of C_l^{gg} for the four redshift bins of WSC.

Table 3
Summary of Bias Results for WSC

z_p Range	B. Stölzner et al. (2018) fix cosmo.	B. Stölzner et al. (2018) marg. cosmo.	H. S. Xavier et al. (2019)	J. A. Peacock & M. Bilicki (2018)	
$0.1 < z_p < 0.2$	0.88 ± 0.03	0.83 ± 0.026	1.43	1.106	
$0.2 < z_p < 0.3$	0.80 ± 0.02	0.99 ± 0.034	1.2	1.175	
$0.3 < z_p < 0.4$	1.26	1.548	
$0.4 < z_p < 0.5$	
Default	$10 < \ell < 70$	Following C. P. Novaes et al. (2018) $10 < \ell < 70$	Following M. Rafiei-Ravandi et al. (2021) $10 < \ell < 70$	unWISE mask $10 < \ell < 70$	SVM $P > 0.9$ $10 < \ell < 70$
0.66 ± 0.44	1.10 ± 0.051	1.08 ± 0.051	1.09 ± 0.045	0.99 ± 0.056	1.06 ± 0.045
1.35 ± 0.66	1.30 ± 0.047	1.41 ± 0.043	1.55 ± 0.040	1.14 ± 0.054	1.57 ± 0.038
1.78 ± 0.87	1.66 ± 0.064	1.78 ± 0.06	1.89 ± 0.050	1.48 ± 0.068	1.86 ± 0.098
2.33 ± 1.10	2.36 ± 0.41	3.60 ± 1.41	4.04 ± 0.21	3.75 ± 0.19	4.59 ± 0.28

Note. Results from the literature are at the top, and our results are at the bottom with several variations in the sample selection or scale cut.

A.2. Results

We compare our bias measurement to previous results in Table 2 for 2MPZ. For 2MPZ, the precise sample selection is slightly different between analyses: B. Stölzner et al. (2018) use $0 < z_{\text{phot}} < 0.105$, A. Balaguera-Antolínez et al. (2018) use $0 < z_{\text{phot}} < 0.08$, J. A. Peacock & M. Bilicki (2018) use $0.05 < z_{\text{phot}} < 0.1$, and D. Alonso et al. (2015) use $0.03 < z_{\text{phot}} < 0.08$ and additionally apply a bright cut of $K_s > 12$. However, despite these subtle differences, the previous results are all broadly consistent with each other and with our result (although the “fixed cosmology” result from B. Stölzner et al. 2018 is significantly low compared to the rest). The differences in errors come mainly from different scales being fit, except for results from A. Balaguera-Antolínez et al. (2018), which have much larger errors because they allow cosmological parameters to vary without including external data (unlike B. Stölzner et al. 2018, who include the Planck likelihood when varying cosmological parameters).

We compare our bias measurement to previous results in Table 3 for WSC. We also test the robustness of our measurements by displaying several different variations in constructing the mask or redshift distribution. For WSC, we also compare to B. Stölzner et al. (2018), although their bins are slightly different than ours ($0.105 < z_p < 0.21$ and $0.21 < z_p < 0.3$). We also compare to results from H. S. Xavier et al. (2019), who use bins of $\Delta z = 0.05$ from 0.15 to 0.35. Therefore, their central redshift differs from ours in the first and third bins (0.175 versus 0.15 and 0.325 versus 0.35); in the second bin, we average their two bins in $0.2 < z_p < 0.3$. Similarly, we also average the $\Delta z = 0.05$ bins of J. A. Peacock & M. Bilicki (2018), and report their result from the $0.3 < z_p < 0.35$ bin in the third row.

Our WSC results have much larger uncertainties than any of the previous results. This is from the combination of our restricted ℓ range ($10 < \ell < 40$) and the fact that we add a template for the imprint of SuperCOSMOS plates on the large-scale power, following N. Koukoufilippas et al. (2020). Over this restricted range in scales, the cosmological contribution is nearly degenerate with the amplitude of the plate template. However, if we consider a larger ℓ range, $10 < \ell < 70$, we can break the degeneracy and achieve much tighter constraints on

the bias. Our results are broadly consistent with previous results, but there are differences at the 10%–20% level. This is likely due to slightly different masks and sample selection; in particular, each work uses a different method to remove stellar contamination from WSC (which is a larger problem than for 2MPZ). We are encouraged that we see the same trend of increasing bias as J. A. Peacock & M. Bilicki (2018).

Appendix B

Construction of Galaxy Mask and Galaxy Catalog Selection

B.1. 2MPZ

2MPZ is derived from the all-sky 2MASS near-infrared extended source catalog (XSC; T. H. Jarrett et al. 2000; M. F. Skrutskie et al. 2006), cross-matched to the infrared AllWISE (E. L. Wright et al. 2010) and optical SuperCOSMOS catalogs (N. C. Hambly et al. 2001a, 2001b, 2001c; J. A. Peacock et al. 2016).

The galaxy masks were carefully constructed to remove areas with large numbers of stars or other systematics that could affect galaxy clustering, either by direct stellar contamination or by correlations, e.g., suppressed galaxy density in regions of high stellar density or extinction. We follow A. Balaguera-Antolínez et al. (2018) to construct the 2MPZ mask, starting by masking low Galactic latitudes ($|b| < 10^\circ$, areas of high galactic extinction ($E(B - V) > 0.3$ from D. J. Schlegel et al. (1998), and areas of high stellar density as estimated from the 2MASS Point Source Catalog ($\log n_{\text{star}} > 3.5$).⁹ We further include manual cutouts around the LMC and SMC, excluding $275^\circ 47 < \text{R.A.} < 285^\circ 47$ and $-37^\circ 89 < \text{decl.} < -27^\circ 89$, and $300^\circ 81 < \text{R.A.} < 304^\circ 81$ and $-46^\circ 33 < \text{decl.} < -42^\circ 33$. Finally, we mask additional areas with low completeness in 2MPZ, determined by comparing the number counts of 2MPZ sources and 2MASS XSC sources (with $K_s < 13.9$) in $\text{NSIDE} = 64$ HEALPixes. We remove pixels with $< 85\%$ completeness, mostly corresponding to areas of lower depth around bright stars. We test variations in the masking procedure (i.e., additionally multiplying by the WSC mask, following D. Alonso et al. 2015, or changing the

⁹ https://www.ipac.caltech.edu/2mass/releases/allsky/doc/sec4_5c.html

completeness threshold to 80% or 90%) and find minimal changes in results.

B.2. WSC

WSC is constructed similarly, but cross-matching AllWISE and SuperCOSMOS only. For WSC, we further apply a color cut of $W1 - W2 > 0.2$ to the publicly available sample to reduce stellar contamination and increase uniformity (H. S. Xavier et al. 2019).

For WSC, we follow the masking procedure of H. S. Xavier et al. (2019). We start with the mask distributed with the WSC data release (M. Bilicki et al. 2016).¹⁰ We additionally mask regions with high extinction ($E(B - V) > 0.10$) and high stellar density (density of stars from Gaia greater than seven times the mean). We additionally test several variations in the masking procedure, adding a mask at low Galactic latitudes following M. Rafiei-Ravandi et al. (2021); adding a mask for WISE bright stars (A. Krolewski et al. 2020); and adding a mask of regions in WISE with high Moon contamination, as determined by HEALPix pixels in which GLADE+ (G. Dálya et al. 2022) is incomplete compared to WSC. We also test variations in the sample selection procedure, i.e., additionally using the SVM catalog of T. Krakowski et al. (2016) to restrict to likely galaxies (C. P. Novaes et al. 2018; M. Rafiei-Ravandi et al. 2021). We

find that these variations generally lead to a scale-independent shift in the amplitude of C_ℓ^{gg} , corresponding to either a change in galaxy bias due to differing populations or a change in the stellar contamination fraction, which is entirely degenerate with bias at $\ell > 10$ where the stellar power spectrum is small. In this regime, the effect of changing stellar contamination is degenerate with bias in both the galaxy auto-spectrum and the galaxy cross-spectrum with GW sources, so it will not cause systematic errors in our modeling.

Appendix C

Validation of the Cross-correlation Pipeline

To validate the cross-correlation pipeline, we apply our method to a randomly distributed galaxy catalog having no spatial correlations. As a result, the GW sources in the GWTC-3 will also not exhibit any spatial correlation with these galaxies. The randomly generated galaxy catalog has a comoving number distribution $n(z)$ matching the galaxy distribution in 2MPZ and WSC. We show the plot for the cross-correlation on H_0 , Ω_m , and the bias parameter in Figure 9. The plot indicates no constraints on the value of the Hubble constant with a random catalog. We have also tested our pipeline with a random catalog with constant $n(z)$ and it shows no constraints on the value of the Hubble constant as well.

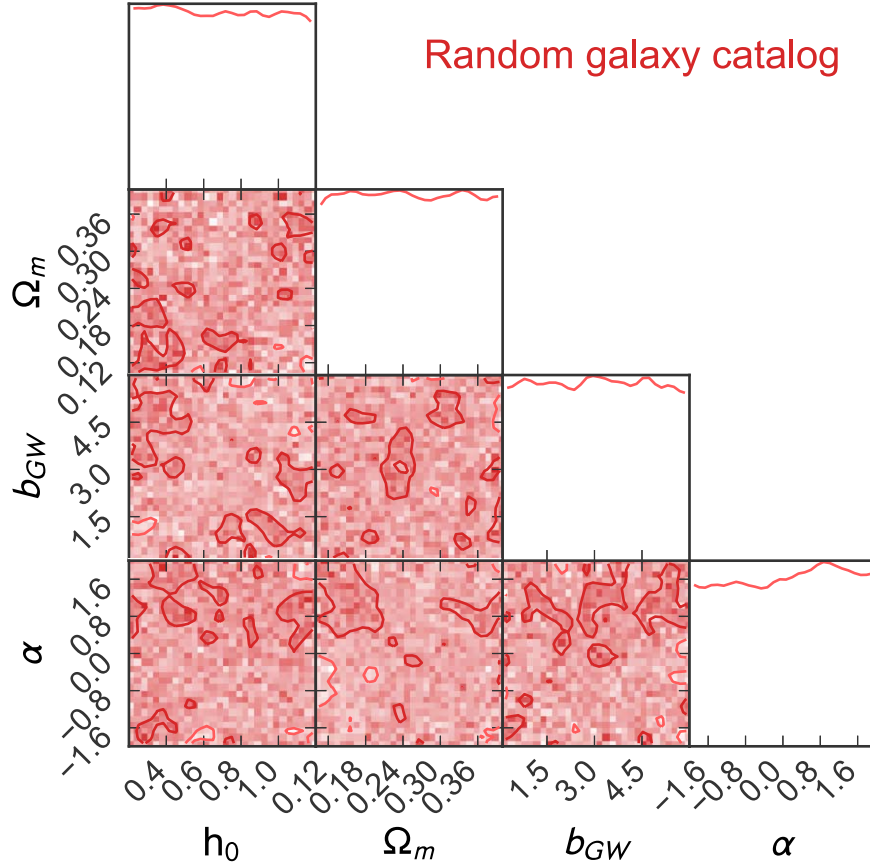


Figure 9. The constraints on the value of H_0 obtained by cross-correlating with a random galaxy catalog having no spatial correlation and with a galaxy distribution $n(z)$ matching 2MPZ and WSC.

¹⁰ <http://ssa.roe.ac.uk/WISExSCOSmask.fits.gz>

ORCID iDs

Benjamin D. Wandelt  <https://orcid.org/0000-0002-5854-8269>

Joseph Silk  <https://orcid.org/0000-0002-1566-8148>

References

- Abbott, B. P., Abbott, R., Abbott, T. D., et al. 2016, *PhRvL*, **116**, 061102
- Abbott, B. P., Abbott, R., Abbott, T. D., et al. 2021, *ApJ*, **909**, 218
- Abbott, R., Abbott, T. D., Abraham, S., et al. 2020, *ApJL*, **896**, L44
- Abbott, R., Abbott, T. D., Acernese, F., et al. 2023, *PhRvX*, **13**, 041039
- Acernese, F., Agathos, M., Agatsuma, K., et al. 2014, *CQGra*, **32**, 024001
- Acernese, F., Agathos, M., Aiello, L., et al. 2019, *PhRvL*, **123**, 231108
- Akutsu, T., Arai, K., Arai, Y., et al. 2021, *PTEP*, **2021**, 05A101
- Alonso, D., Salvador, A. I., Sánchez, F. J., et al. 2015, *MNRAS*, **449**, 670
- Alonso, D., Sanchez, J., & Slosar, A. 2019, *MNRAS*, **484**, 4127
- Astropy Collaboration, Price-Whelan, A. M., Sipőcz, B. M., et al. 2018, *AJ*, **156**, 123
- Astropy Collaboration, Robitaille, T. P., Tollerud, E. J., et al. 2013, *A&A*, **558**, A33
- Balaguera-Antolínez, A., Bilicki, M., Branchini, E., & Postiglione, A. 2018, *MNRAS*, **476**, 1050
- Bera, S., Rana, D., More, S., & Bose, S. 2020, *ApJ*, **902**, 79
- Bilicki, M., Jarrett, T. H., Peacock, J. A., Cluver, M. E., & Steward, L. 2014, *ApJS*, **210**, 9
- Bilicki, M., Peacock, J. A., Jarrett, T. H., et al. 2016, *ApJS*, **225**, 5
- Blanchard, A., Camera, S., Carbone, C., et al. 2020, *A&A*, **642**, A191
- Bocquet, S., & Carter, F. W. 2016, *JOSS*, **1**, 46
- Brown, A. G. A., Vallenari, A., Prusti, T., et al. 2016, *A&A*, **595**, A2
- Cawthon, R., Elvin-Poole, J., Porredon, A., et al. 2022, *MNRAS*, **513**, 5517
- Cigarrán Díaz, C., & Mukherjee, S. 2022, *MNRAS*, **511**, 2782
- Collister, A. A., & Lahav, O. 2004, *PASP*, **116**, 345
- Dainotti, M. G., De Simone, B., Schiavone, T., et al. 2021, *ApJ*, **912**, 150
- Dálya, G., Diaz, R., Bouchet, F. R., et al. 2022, *MNRAS*, **514**, 1403
- Dálya, G., Galgóczi, G., Dobos, L., et al. 2018, *MNRAS*, **479**, 2374
- DESI Collaboration, Aghamousa, A., Aguilar, J., et al. 2016, arXiv:1611.00036
- Di Valentino, E., Mena, O., Pan, S., et al. 2021, *CQGra*, **38**, 153001
- Doré, O., Werner, M. W., Ashby, M. L. N., et al. 2018, arXiv:1805.05489
- Ezquiaga, J. M., & Holz, D. E. 2022, *PhRvL*, **129**, 061102
- Farmer, R., Renzo, M., de Mink, S. E., Marchant, P., & Justham, S. 2019, *ApJ*, **887**, 53
- Farr, W. M., Fishbach, M., Ye, J., & Holz, D. E. 2019, *ApJL*, **883**, L42
- Finke, A., Foffa, S., Iacovelli, F., Maggiore, M., & Mancarella, M. 2021, *JCAP*, **2021**, 026
- Foreman-Mackey, D., Hogg, D. W., Lang, D., & Goodman, J. 2013, *PASP*, **125**, 306
- Gatti, M., Giannini, G., Bernstein, G. M., et al. 2022, *MNRAS*, **510**, 1223
- Górski, K. M., Hivon, E., Banday, A. J., et al. 2005, *ApJ*, **622**, 759
- Grain, J., Tristram, M., & Stompor, R. 2009, *PhRvD*, **79**, 123515
- Hambly, N. C., Davenhall, A. C., Irwin, M. J., & MacGillivray, H. T. 2001a, *MNRAS*, **326**, 1315
- Hambly, N. C., Irwin, M. J., & MacGillivray, H. T. 2001b, *MNRAS*, **326**, 1295
- Hambly, N. C., MacGillivray, H. T., Read, M. A., et al. 2001c, *MNRAS*, **326**, 1279
- Heymans, C., Tröster, T., Asgari, M., et al. 2021, *A&A*, **646**, A140
- Hivon, E., Górski, K. M., Netterfield, C. B., et al. 2002, *ApJ*, **567**, 2
- Hunter, J. D. 2007, *CSE*, **9**, 90
- Jarrett, T. H., Chester, T., Cutri, R., et al. 2000, *AJ*, **119**, 2498
- Jones, E., Oliphant, T., Peterson, P., et al. 2001, SciPy: Open Source Scientific Tools for Python, <http://www.scipy.org/>
- Kagra Collaboration, Akutsu, T., Ando, M., et al. 2019, *NatAs*, **3**, 35
- Koukoufilippas, N., Alonso, D., Bilicki, M., & Peacock, J. A. 2020, *MNRAS*, **491**, 5464
- Krakowski, T., Malek, K., Bilicki, M., et al. 2016, *A&A*, **596**, A39
- Krolewski, A., Ferraro, S., Schlafly, E. F., & White, M. 2020, *JCAP*, **2020**, 047
- LIGO Scientific Collaboration, Aasi, J., Abbott, B. P., et al. 2015, *CQGra*, **32**, 074001
- LSST Science Collaboration, Abell, P. A., Allison, J., et al. 2009, arXiv:0912.0201
- Martynov, D. V., Hall, E. D., Abbott, B. P., et al. 2016, *PhRvD*, **93**, 112004
- Mastrogiovanni, S., Leyde, K., Karathanasis, C., et al. 2021, *PhRvD*, **104**, 062009
- Menard, B., Scranton, R., Schmidt, S., et al. 2013, arXiv:1303.4722
- Mukherjee, S. 2022, *MNRAS*, **515**, 5495
- Mukherjee, S., Lavaux, G., Bouchet, F. R., et al. 2021a, *A&A*, **646**, A65
- Mukherjee, S., & Wandelt, B. D. 2018, arXiv:1808.06615
- Mukherjee, S., Wandelt, B. D., Nissanke, S. M., & Silvestri, A. 2021b, *PhRvD*, **103**, 043520
- Mukherjee, S., Wandelt, B. D., & Silk, J. 2020, *MNRAS*, **494**, 1956
- Mukherjee, S., Wandelt, B. D., & Silk, J. 2021c, *MNRAS*, **502**, 1136
- Newman, J. A. 2008, *ApJ*, **684**, 88
- Novaes, C. P., Bernui, A., Xavier, H. S., & Marques, G. A. 2018, *MNRAS*, **478**, 3253
- Oguri, M. 2016, *PhRvD*, **93**, 083511
- Palmese, A., Bom, C. R., Mucesh, S., & Hartley, W. G. 2023, *ApJ*, **943**, 56
- Peacock, J. A., & Bilicki, M. 2018, *MNRAS*, **481**, 1133
- Peacock, J. A., Hambly, N. C., Bilicki, M., et al. 2016, *MNRAS*, **462**, 2085
- Pérez, F., & Granger, B. E. 2007, *CSE*, **9**, 21
- Planck Collaboration, Aghanim, N., Akrami, Y., et al. 2020, *A&A*, **641**, A6
- Rafiei-Ravandi, M., Smith, K. M., Li, D., et al. 2021, *ApJ*, **922**, 42
- Rau, M. M., Dalal, R., Zhang, T., et al. 2023, *MNRAS*, **524**, 5109
- Riess, A. G., Casertano, S., Yuan, W., Macri, L. M., & Scolnic, D. 2019, *ApJ*, **876**, 85
- Riess, A. G., Yuan, W., Macri, L. M., et al. 2022, *ApJL*, **934**, L7
- Schlegel, D. J., Finkbeiner, D. P., & Davis, M. 1998, *ApJ*, **500**, 525
- Schmidt, S. J., Menard, B., Scranton, R., Morrison, C., & McBride, C. K. 2013, *MNRAS*, **431**, 3307
- Schutz, B. F. 1986, *Natur*, **323**, 310
- Skrutskie, M. F., Cutri, R. M., Stiening, R., et al. 2006, *AJ*, **131**, 1163
- Soares-Santos, M., Palmese, A., Hartley, W., et al. 2019, *ApJL*, **876**, L7
- Stözlner, B., Cuoco, A., Lesgourgues, J., & Bilicki, M. 2018, *PhRvD*, **97**, 063506
- Takahashi, R., Sato, M., Nishimichi, T., Taruya, A., & Oguri, M. 2012, *ApJ*, **761**, 152
- Taylor, S. R., Gair, J. R., & Mandel, I. 2012, *PhRvD*, **85**, 023535
- van der Walt, S., Colbert, S. C., & Varoquaux, G. 2011, *CSE*, **13**, 22
- Verde, L., Treu, T., & Riess, A. 2019, *NatAs*, **3**, 891
- Wright, E. L., Eisenhardt, P. R. M., Mainzer, A. K., et al. 2010, *AJ*, **140**, 1868
- Xavier, H. S., Costa-Duarte, M. V., Balaguera-Antolínez, A., & Bilicki, M. 2019, *JCAP*, **2019**, 037
- Zhou, R., Newman, J. A., Mao, Y.-Y., et al. 2021, *MNRAS*, **501**, 3309
- Zonca, A., Singer, L., Lenz, D., et al. 2019, *JOSS*, **4**, 1298